ISBN: 978-3-95450-208-0 doi:10.18429/JACoW-IPAC2019-TUPGW082

IMPEDANCE OF THE FLANGE JOINTS WITH THE RF CONTACT SPRING IN NSLS-II*

A. Blednykh†, B. Bacha, G. Bassi, C. Hetzel, B. Kosciuk, V. Smaluk, T. Shaftan, G. Wang
BNL, NSLS-II, Upton, NY, USA

Abstract

Since the beginning of the NSLS-II commissioning, temperature of the vacuum components has been monitored by the Resistance Temperature Detectors located predominantly outside of the vacuum enclosure and attached to the chamber body. Mapping the temperature is helpful to control overheating of the vacuum components around the ring especially during the current ramp-up. The average current of 475mA has been achieved with two main 500MHz RF cavities and w/o harmonic cavities. Effect of the RF shielded flanges on local heat and on the longitudinal beam dynamics is discussed in details.

INTRODUCTION

The unperturbed energy spread σ_δ at low single bunch current I_0 in the NSLS-II storage ring can be varied by closing and opening the magnet gaps of three 7m damping wigglers installed in Cell 08, 18, 28 [1]. The Bare Lattice (BL) corresponds to all IDs magnet gaps open. The predicted energy spread at $V_{RF} = 3.4MV$, determined by the Bending Magnet (BM), is $\sigma_\delta = 0.5 \times 10^{-3}$. The expected increase of the energy spread by closing one Damping Wiggler (1DW) and three Damping Wigglers (3DWs), is $\sigma_\delta = 0.71 \times 10^{-3}$ and $\sigma_\delta = 0.87 \times 10^{-3}$ respectively. The main storage ring parameters to estimate the collective effects are given in Table 1, where the RF voltage is induced by two superconducting 500MHz CESR-B RF cavities installed back-to-back in Cell 24 with a capability to deliver a maximum total RF voltage of $V_{RF} = 3.8MV$ with the present RF power couplers design. A second RF straight section is reserved for two more RF cavities.

Table 1: NSLS-II Parameters for the Collective Effects Characterization

Energy	$E_0(GeV)$	3		
Revolution period	$T_0(\mu s)$	2.6		
Momentum compaction	α	3.7 x 10^{-4}		
RF voltage	$V_{RF}(MV)$	3.4		
Synchrotron tune	ν_s	9.2 x 10^{-3}		
		BL	1DW	3DW
Energy loss	$U(keV)$	287	400	674
Damping time	$\tau_x, \tau_s\ (ms)$	54, 27	40, 20	23,11.5
Energy spread	σ_δ (%)	0.05	0.071	0.087
Horizontal Emittance	$\varepsilon_x\ (nm)$	2.1	1.4	0.9
Bunch length (at low current)	$\sigma_s\ (mm)$	2.5	3.5	4.3

LOCAL OVERHEATING

The RF contact spring (Fig. 1) has been designed for installation in the area between two flange joints to eliminate the large cavity effect generating wakefield/impedances. To stay securely, the RF contact spring is placed in one of the flanges with trapezoidal groove. Due to the RF spring installation procedure and a bit larger gaps between two groups of flanges, the local overheating appeared at different locations of the NSLS-II storage ring, predominately in the straight sections. The local overheating has been measured by the thermal Infrared (IR) camera (Fig. 2) and the Resistance Temperature Detector (RTD) sensors (Fig. 3), installed on the surface of the flange joints.

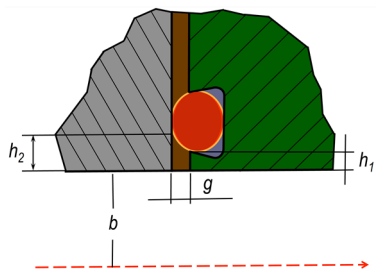

Figure 1: The RF contact spring placed between flanges.

Figure 2: Thermal image of the attached bellows to the flange of the vacuum chamber made by the FLIR AX8 infrared camera, where the local overheating appeared.

The gap being closed by the RF spring varies at different locations around the storage ring. Where the gap g is at its maximum ($g \approx 1.2mm$), proper installation of the RF spring is critical to ensure good contact between adjoining vacuum flanges. There are multiple flange joints in the straight sections that have this geometry which explains the high concentration of hot flanges in this area. Figure 4 shows an example of a spring which has not been installed correctly. The difference in the height of the spring on either side of the beam aperture becomes clear when a straight edge is placed across the opening. Figure 5 shows the imprint of the spring contact on the adjoining flange when the RF spring is not installed correctly. This flange joint was one of the locations getting hot during operations

ISBN: 978-3-95450-208-0 doi:10.18429/JACoW-IPAC2019-TUPGW082

(Fig. 3). Once the RF spring was changed and properly installed, the flange temperature returned to normal.

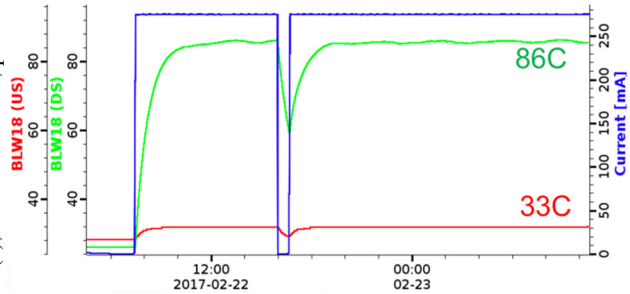

Figure 3: Experimental data of temperature rise on the downstream and upstream side of the bellows at $I_{av} = 275mA$ within $M = 1005$ bunches and $V_{RF} = 3MV$ corresponding to an extended bunch length of $\sigma_s \approx 5.4mm$.

Figure 4: Flange image of the bellows with trapezoidal grove and the RF contact spring at place after disassembling.

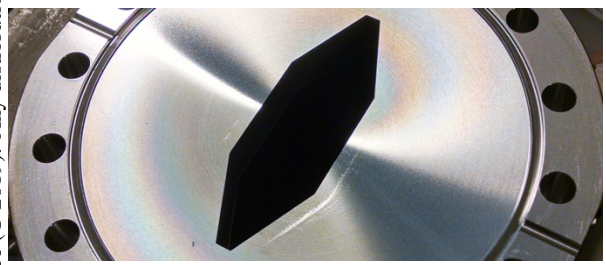

Figure 5: Surface image of the flange, which was attached to the bellows flange. There is a scratch on the surface, where the RF spring has a good contact.

The loss factor and imaginary part of the longitudinal impedance at low frequency divided by $n = \omega/\omega_0$ are presented in Table 2 for the flange geometries with: 100% gap around the octagonal shape, 50% gap, where only half-aperture has a good contact with the RF contact spring and zero gap, when the RF contact spring has a good contact with the whole surface around the aperture, where the small cavity with parameters h_2 and g can be considered (Fig. 1). The loss factor of the octagonal "zero gap" flange joints is 1.4 times the circular value $k_{loss,oct} = 1.4k_{loss,cir}$.

Table 2: The Numerically Simulated Loss Factor and Imaginary Part of the Longitudinal Impedance

GdfidL	100% gap	50% gap	Zero gap	Circular Zero gap
k_{loss}, mV/pC	32	16	1.8	1.3
$\left(\frac{ImZ_{\|\|}}{n}\right)_0$, mΩ	0.6	0.3	0.08	0.07

ENERGY SPREAD

Based on the experience with the RF contact springs in NSLS-II [2,3], the height h_2 can be varied from flange to flange, $h_2 \sim 2.6mm$ if the springs loops are oriented perpendicularly to the attached surface (best case scenario) and $h_2 > 2.6mm$ if the RF contact spring loops are skewed manually or during installation. In Fig. 6 we compare the energy spread σ_δ numerically calculated by the SPACE code [4] versus experimental data collected by the Synchrotron Light Monitor (SLM) camera in NSLS-II. We also discuss how sensitive the simulated microwave beam pattern behaviour on the geometric parameters h_2 and g can be. The total longitudinal wakepotential $W_{||,tot}(s)$ has been generated including 739 flange joints with $h_2 = 3.2mm$ and $h_2 = 2.6mm$. The results for the combination of 339 flange joints with $h_2 = 3.2mm$ and 400 flange joints with $h_2 = 2.6mm$ are presented in Fig. 6. Given the difficulty to know the real geometric dimensions of each individual flange joints, we combined flange joints into two groups with geometric dimensions $h_2 = 2.6mm$, $g = 0.9mm$ and $h_2 = 3.2mm$, $g = 1.0mm$ and the results are summed. The microwave instability threshold (I_{th}) is determined from Fig. 6 by noting that below I_{th}, the energy distribution is current independent. The orange trace represents the SLM experimental data, where the energy spread is obtained from the measured horizontal beam size σ_x as a function of single bunch current $\sigma_x(I_0)$ with $\beta_x = 2.77m$, $\eta_x = 0.13m$ and $\varepsilon_x = 0.9nm$ for the 3DW lattice. The purple and orange traces are the numerically simulated results by the SPACE code. The longitudinal microwave instability threshold is $I_{th} = 1.2mA$ at $V_{RF} = 3.4MV$, which is larger than the current per bunch during regular beam operation at $I_{av} = 500mA$ within $M = 1000$ bunches.

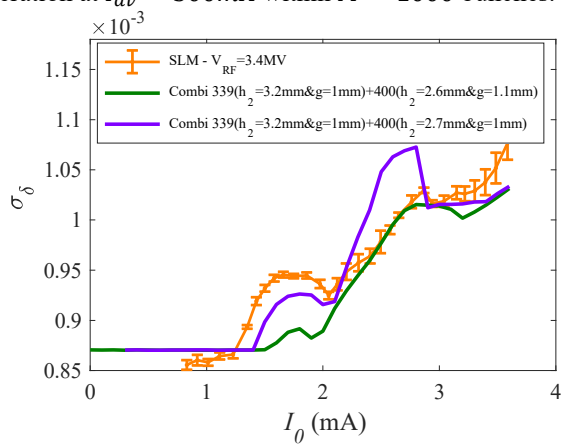

Figure 6: Energy spread change vs. single-bunch current for 739 RF shielded flange joints at $V_{RF} = 3.4MV$. The purple and green traces are numerically simulated data. The σ_δ measured data (orange trace) at $V_{RF} = 3.4MV$ are shown for comparison.

Despite the good agreement shown in Fig. 6 between measurements and simulations of σ_δ a discrepancy has been observed in the comparison of the bunch length (σ_τ), as shown in Fig. 7 at $V_{RF} = 3MV$. The blue dots correspond to the streak camera measurements for the regular 3DW

ISBN: 978-3-95450-208-0 doi:10.18429/JACoW-IPAC2019-TUPGW082

lattice and the purple solid trace corresponds to the numerically simulated results by the SPACE code. We are presently investigating the reason why we can reproduce well the energy spread behaviour while, the bunch lengthening slopes differ by a factor of 1.4. The low-frequency part of the longitudinal impedance, especially the imaginary part needs to be further investigated and analysed in detail to resolve and understand the difference between the results. We believe that with a streak camera resolution better than $0.5ps$ we will be able to detect changes in bunch length, where the beam becomes unstable, especially at high enough RF voltage.

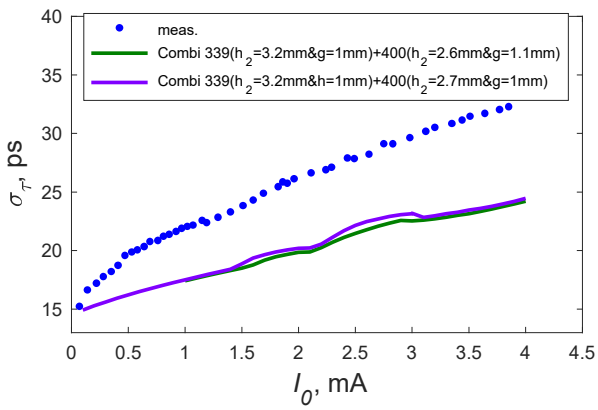

Figure 7: Bunch length dependence on the single bunch current. The experimental data are shown with blue points. The purple and green traces are the numerically simulated results.

The frequency spectrum of the total NSLS-II longitudinal impedance is presented in Fig. 8 (green trace) and Fig. 9 (purple trace) up to $300GHz$. There are several observable broad-band peaks at different frequencies, $\sim 25GHz$, $\sim 90GHz$, $\sim 180GHz$, $\sim 220GHz$,... . The main spectral peak at $f \sim 27GHz$ has the highest magnitude, $ReZ_{||} = 13k\Omega$, and it is predominantly due to a big number of RF shielded flanges assembled with RF contact spring between flanges. The frequency spectrum is changed significantly by excluding the contribution of the 739 flanges (Fig. 8, orange trace and Fig. 9 magenta trace) from the total impedance. Engineering design of the RF shielded flanges with "no gap" will be beneficial to increase the microwave instability threshold.

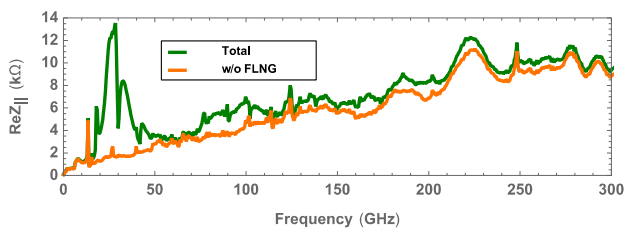

Figure 8: The real part of the longitudinal impedance up to $300GHz$ frequency range. Green trace is the total NSLS-II longitudinal impedance. Orange trace is $ReZ_{||}$ without contribution of the RF sealed flanges.

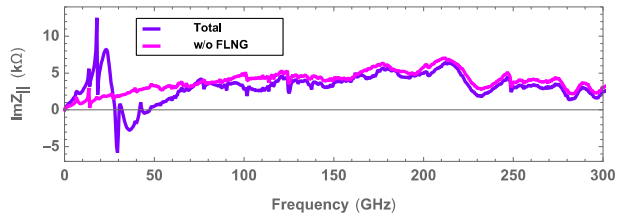

Figure 9: The imaginary part of the longitudinal impedance up to $300GHz$ frequency range. Purple trace is the total NSLS-II longitudinal impedance. Magenta trace is $ImZ_{||}$ without contribution of the RF sealed flanges.

The numerical simulation of σ_δ without contribution of the RF shielded flanges to the total impedance of the storage ring, shows that the instability threshold current is increased to a value higher than 15mA (Fig. 10).

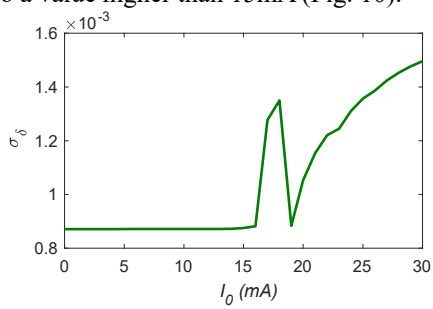

Figure 10: Numerically simulated σ_δ vs. single-bunch current for the impedance model without RF shielded flanges.

CONCLUSION

The main contribution to the microwave instability threshold has been determined to be due to the geometric dimensions of the 739 RF shielded flange joints. The single-bunch longitudinal instability thresholds have been confirmed with three different measurement techniques [5]. The local overheating occurs where the RF contact spring does not have a good contact with a surface of the flange, partly or completely. The flange temperature returned to normal after RF spring replacement and changes made in installation procedure.

REFERENCES

[1] Brookhaven National Laboratory, 2006, NSLS-II Conceptual Design Report.

[2] S. Seletskiy, G. Bassi, J. Bengtsson, A. Blednykh, E. Blum, W. Cheng, J. Choi, R. Fliller, W. Guo, R. Heese, Y. Hidaka, S. Kramer, Y. Li, B. Podobedov, T. Shaftan, G. Wang, F. Willeke, L. Yang, X. Yang, "Experience with first turns commissioning in NSLS-II storage ring," Proceedings of IPAC2015, Richmond, VA, USA.

[3] A. Blednykh, "First Collective Effects Measurements in NSLS-II", Low Emittance Rings 2014 Workshop, Sep. 17-19, 2014, Frascati, Italy.

[4] G. Bassi, A. Blednykh and V. Smaluk, Phys. Rev. Acc. and Beams 19, 024401 (2016).

[5] A. Blednykh, B. Bacha, G. Bassi, W. Cheng, O. Chubar, A. Derbenev, R. Lindberg, M. Rakitin, V. Smaluk, M. Zhernen-

ISBN: 978-3-95450-208-0 doi:10.18429/JACoW-IPAC2019-TUPGW082

kov, Yu-chen Karen Chen-Wiegart and L. Wiegart, "New aspects of longitudinal instabilities in electron storage rings", Scientific Reports volume 8, Article number: 11918 (2018).